

Article

Tensile Properties of a Non-Equiatomic Ni–Co–V Medium Entropy Alloy at Cryogenic Temperature

Dawei Zhou ¹, Caijuan Shi ^{2,*}, Caixia Wang ¹, Ruixin Sheng ¹, Weidong Li ^{3,*} and Yang Tong ^{1,*}

¹ Institute for Advanced Studies in Precision Materials, Yantai University, Yantai 264005, China; calawayzhou@s.ytu.edu.cn (D.Z.); wangcaixia@s.ytu.edu.cn (C.W.); shengruixin@s.ytu.edu.cn (R.S.)

² Synchrotron Radiation Facility, Institute of High Energy Physics, Chinese Academy of Sciences, Beijing 100049, China

³ Beijing Advanced Innovation Center for Materials Genome Engineering, University of Science and Technology Beijing, Beijing 100083, China

* Correspondence: shicj@ihep.ac.cn (C.S.); wli20@utk.edu (W.L.); yt1@ytu.edu.cn (Y.T.)

Abstract: The development of strong and ductile alloys for application in cryogenic temperatures has long been sought after. In this work, we have developed a face-centered cubic Ni₁₀Co_{56.5}V_{33.5} multi-principal element alloy (MPEA) that exhibits a balanced combination of high strength and good ductility at 77 K, based on the considerations of large local lattice distortion (LLD) and low stacking fault energy. The small-grained Ni₁₀Co_{56.5}V_{33.5} MPEA exhibits a yield strength of 1400 MPa and an ultimate tensile strength of 1890 MPa, while preserving a good ductility of 23%. Moreover, precession electron diffraction and transmission electron microscopy revealed multiple deformation mechanisms, including wavy dislocations, atypically severely twisted dislocation bands, hierarchical stacking faults, and deformation twins, which are implicated in the alloy's outstanding mechanical performance. These insights offer a strategic guide for the design of strong and ductile alloys, particularly for utilization in extreme environments.

Keywords: multi-principal element alloy; tensile properties; transmission electron microscopy; density functional theory; deformation mechanism



Citation: Zhou, D.; Shi, C.; Wang, C.; Sheng, R.; Li, W.; Tong, Y. Tensile Properties of a Non-Equiatomic Ni–Co–V Medium Entropy Alloy at Cryogenic Temperature. *Metals* **2024**, *14*, 590. <https://doi.org/10.3390/met14050590>

Academic Editor: Cristian Ciobanu

Received: 10 April 2024

Revised: 30 April 2024

Accepted: 15 May 2024

Published: 17 May 2024



Copyright: © 2024 by the authors. Licensee MDPI, Basel, Switzerland. This article is an open access article distributed under the terms and conditions of the Creative Commons Attribution (CC BY) license (<https://creativecommons.org/licenses/by/4.0/>).

1. Introduction

The development of multi-principal element alloys (MPEAs), a novel category of solid-solution alloys with multiple elements in equimolar or near-equimolar proportions [1,2], has fundamentally transformed alloy design by shifting from the corners of phase diagrams to their central regions [3–6]. The new alloy design strategy has led to the discovery of novel alloys that surpass the properties exhibited by conventional single-principal element alloys [7–9]. Notably, a recent study by Liu et al. [9] reports a record-high fracture toughness in the equiatomic NiCoCr MPEA at the cryogenic temperature of 20 K, 540 MPa·m^{1/2}. Due to their remarkable capacity to maintain or even enhance both strength and ductility upon cooling to cryogenic temperatures [10–12], the single-phase face-centered-cubic (FCC) MPEAs have shown a great potential for application in extreme environments. This is particularly critical as most alloys are known to experience a reduction in toughness at decreased temperatures, a phenomenon that becomes more pronounced within the cryogenic temperature domain [13,14].

Driven by the practical requirements of reducing mass and energy consumption, the design of ultra-strong and ductile MPEAs remains a continuous endeavor. However, MPEAs with the FCC structure typically manifest low yield strength. Recently, the maximization of local lattice distortion (LLD) [15–19] has been proposed as a new strategy for designing ultra-strong single-phase MPEAs. LLD, considered as one of the core effects in MPEAs, originates from the large atomic size mismatch among constituents in MPEAs [3]. Sohn et al. [15] have reported that the single-phase NiCoV MPEA with a severe

LLD, exhibits an exceptional yield strength of ~1 GPa at room temperature. Theoretical solid-solution strengthening models have been developed from the perspective of LLD. Okamoto et al. [20] have reported that the yield stress at 0 K for the CoCrFeNiMn and its derivative quaternary and ternary equiatomic MPEAs is solely governed by the average static displacements of constituents. Varvenne et al. [21] proposed a solute-dislocation interaction model based on the atomic volume mismatch parameter, which successfully predicted the yield strength of FCC CoCrFeNiMn and CoCrFeNi MPEAs. Therefore, increasing LLD is critical for the design of strong MPEAs.

MPEAs with severe LLD, e.g., the equiatomic FCC NiCoV [15] and body-centered cubic NbTaTiVZr [16], often exhibit dislocation-controlled deformation mechanism, and the strength–ductility trade-off in such MPEAs is often observed due to the reduced mobility of dislocations at lower temperatures. However, the introduction of multiple deformation mechanisms is an effective strategy by which to enhance the ductility of MPEAs, and this can be achieved by reducing the stacking fault energy (SFE) [22–24]. When the SFE is sufficiently low, dislocation cross-slip is suppressed while dislocation decomposition and even twinning is promoted [25]. The reported toughest equiatomic NiCoCr is a typical MPEA with multiple deformation mechanisms, including planar dislocation slip, stacking faults (SFs), and deformation twins [26,27].

The equiatomic NiCoV MPEA has garnered significant interest due to its remarkable tensile properties at both room and cryogenic temperatures [12,15]. Yang et al. [28] have discovered that, with the decrease of temperature, the equiatomic NiCoV MPEA exhibits enhanced strength and ductility. They found that this equiatomic MPEA retains planar dislocation slip as the predominant deformation mechanism at 77 K [28]. This is attributed to its relatively low SFE and high friction stress due to large LLD, which promotes the dissociation of full dislocations and retards dislocation motion at cryogenic temperature. However, the equiatomic NiCoV MPEA may not be the optimal composition, especially regarding ductility, predominantly characterized by a dislocation-controlled deformation mechanism. Consequently, an adjustment of the Ni–Co–V atomic ratio, aimed at reducing SFE to introduce multiple deformation mechanisms while simultaneously preserving a high degree of LLD, emerges as a viable approach for enhancing the alloy's mechanical performance. In the present work, we developed a non-equiatomic Ni₁₀Co_{56.5}V_{33.5} MPEA based on the considerations of optimizing SFE and LLD. Meanwhile, to optimize its mechanical performance, we embarked on an investigation of the grain size impact on the tensile properties of the Ni₁₀Co_{56.5}V_{33.5} MPEA at cryogenic temperature. This study integrated both computational predictions and experimental characterizations, facilitating a comprehensive analysis of the MPEA's microstructure feature and deformation mechanisms.

2. Methodology

2.1. Sample Preparation

The Ni₁₀Co_{56.5}V_{33.5} alloy was synthesized by arc melting high-purity Ni, Co, and V metals ($\geq 99.9\%$) in an atmosphere of high-purity argon. The ingot was flipped and remelted five times to ensure compositional homogeneity before suction casting into a copper mold with dimensions of $8 \times 8 \times 80 \text{ mm}^3$. The cast rods were vacuum-sealed in a quartz tube and homogenized at 1473 K for 24 h, followed by water quenching to preserve the high-temperature state. The homogenized rods were then cold-rolled longitudinally from a thickness of 8.0 to 1.5 mm, achieving a thickness reduction of 80%. Flat dog-bone-shaped tensile specimens with a gauge length of 20 mm and a thickness of 1.5 mm were wire-cut from the cold-rolled plate along the rolling direction. Recrystallization heat treatment was then conducted on three tensile specimens at 1473 K for 10 min, 1373 K for 3 min and 1473 K for 1 min, respectively, to obtain different grain sizes. Figure 1 shows the heat treatment histories of these samples. These recrystallized tensile samples are henceforth denoted as S1 to S3. After fine polishing the surfaces with 2000 grit sandpaper, all tensile samples were subjected to tensile tests at a strain rate of $1 \times 10^{-3} \text{ s}^{-1}$ using an SENS CMT-5105

10T tensile machine (Shenzhen, China) at the cryogenic temperature of 77 K in a liquid nitrogen environment.

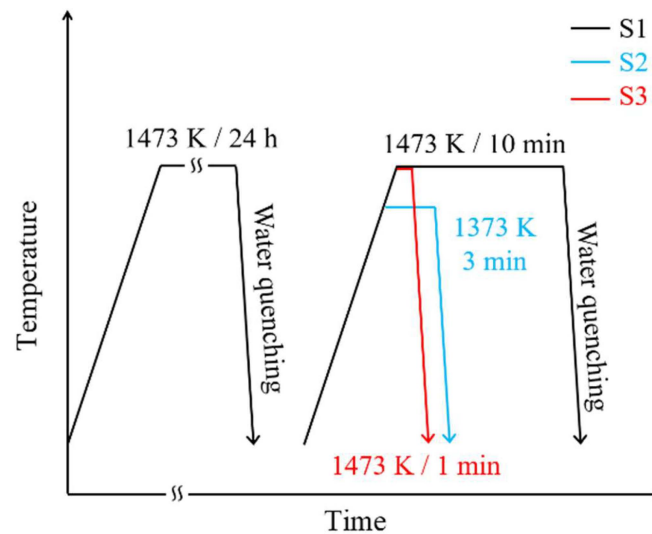


Figure 1. Heat treatment process in sample preparation.

2.2. Calculations

To examine LLD, first principles calculations were performed using density functional theory (DFT) implemented in the Vienna ab initio simulation package (VASP) code [29]. The projected augmented wave (PAW) method was employed in combination with the Perdew–Burke–Ernzerhof (PBE) [30] generalized gradient approximation [31] for the exchange–correlation potential. A Γ -centered $2 \times 2 \times 2$ k-point grid was used for Brillouin zone sampling. Wavefunctions were expanded in a plane–wave basis with a kinetic energy cutoff of 350 eV, and the electronic convergence criterion was set to 1.0×10^{-5} eV. Ionic positions were relaxed until residual ionic forces were below 10^{-3} eV/Å. For the DFT calculations, a supercell containing 108 atoms was constructed based on the special quasi-random structure (SQS) approach [32].

2.3. Characterization

High-energy X-ray diffraction (HEXRD) analysis was conducted for phase identification at Beamline 3W1A, Beijing Synchrotron Radiation Research Institute. The incident X-ray energy was set to 60.16 keV, corresponding to a wavelength of 0.2061 Å. Diffraction data collection was performed using a 2-dimensional detector positioned 862 mm away from the sample stage along the X-ray beam path.

For microstructural characterization, a field-emission scanning electron microscope (SEM, TESCAN AMBER, Brno, Czech Republic) equipped with an electron backscattered diffraction probe (EBSD, OXFORD VEGA, Abingdon, UK) and a transmission electron microscope (TEM, Talos F200X G2) were utilized. Precession electron diffraction (PED) analysis, undertaken to achieve nanoscale EBSD resolution, was conducted using a TEM (FEI Tecnai F30, Waltham, MA, USA) equipped with a NanoMEGAS detector. The preparation of EBSD samples involved grinding with sandpapers of grit ranging from 800 to 2000, followed by mechanical polishing with a 0.05 μm SiO_2 suspension and electropolishing in a solution with a volume ratio of H_2SO_4 to CH_3OH of 1:4. TEM samples were prepared using a twin-jet technique with a 10% volume fraction perchloric acid alcohol solution, applying a voltage of 20 V and maintaining a temperature of 263 K.

2.4. AI tool

AI tool was utilized solely for the purpose of grammar and syntax checking in the manuscript. The originality, validity, and integrity of the content of their manuscript was ensured without any assistance from AI tool.

3. Results

3.1. Microstructure

Figure 2a shows the calculated ternary phase diagram for the Ni–Co–V system at 1373 K. A red dot near the edge of the single FCC region marks the composition of the alloy under investigation. The choice of composition aims to achieve a balance between ductility and strength. Vanadium effectively enhances strength in Ni-based alloys [33] while the incorporation of Co into Ni decreases the SFE [34], promoting the formation of SFs and deformation twins. Figure 2b presents the HEXRD profiles of the selected alloy subjected to various recrystallization heat treatments. The predominant phase is observed to have an FCC structure and a minor fraction of the σ phase is identified close to the results of the thermodynamic calculation in Figure 2a. Quantitative XRD phase analysis reveals that the volume fraction of the σ phase is rather small, with 2.0%, 3.0% and 2.7% for S1, S2 and S3, respectively.

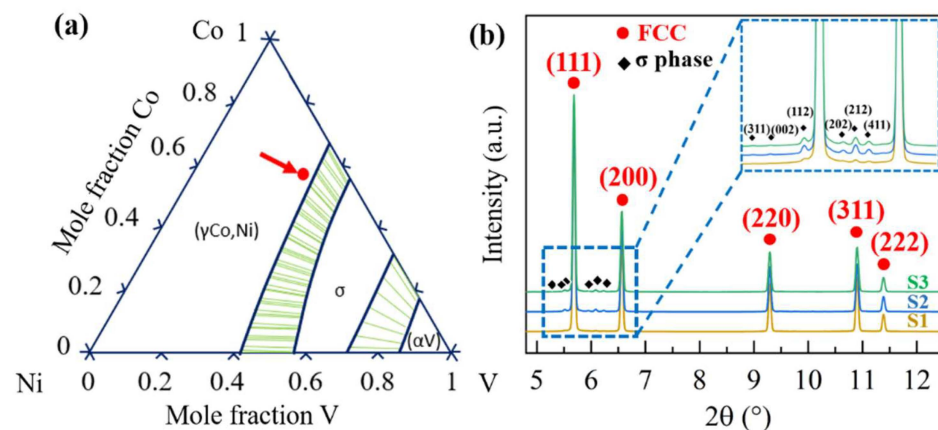


Figure 2. (a) Ternary phase diagram of Ni–Co–V at 1373 K. Reprinted with permission from ref. [35]. Copyright 2019, Elsevier Ltd. The red dot indicates the studied $\text{Ni}_{10}\text{Co}_{56.5}\text{V}_{33.5}$ MPEA. (b) HEXRD profiles of samples after different recrystallization heat treatment. The inset is an enlarged view of diffraction peaks of the minor σ phase.

Figure 3 shows the inverse pole figures (IPFs) of the recrystallized samples. All samples were fully recrystallized with an equiaxed grain structure. However, the grain size distribution varies dramatically between the S1 sample and the others. The S1 sample exhibits a relatively homogeneous grain size, whereas samples S2 and S3 display a heterogeneous microstructure characterized by a mix of large and small grains, as demonstrated by the grain size distribution histograms in Figure 3. The average grain sizes are $16.0\ \mu\text{m}$ for sample S1, $5.1\ \mu\text{m}$ for sample S2 and $4.5\ \mu\text{m}$ for sample S3. Additionally, a significant number of annealing twins is observed in the S1 sample. In contrast, the density of such annealing twins significantly decreases in the S2 and S3 samples.

We further examined the σ phase in these recrystallized samples. TEM analysis of the σ phase in the large-grained S1 sample is presented in Figure 4. The high angle annular dark field (HAADF) image in Figure 4a reveals that small spherical σ precipitates predominantly exist within the grain interiors with an average diameter of $\sim 130\ \text{nm}$, while negligible σ precipitates are sparsely distributed at grain boundaries. The high-resolution transmission electron microscope (HRTEM) image in Figure 4b, taken along the [001] zone axis of the σ phase, further reveals a semi-coherent interface between small σ precipitate and the matrix. The fast Fourier transform (FFT) image in the inset of Figure 4b shows a

typical diffraction pattern of the σ phase. Additionally, the selected area electron diffraction (SAED) pattern (Figure 4c) closely matches the calculated diffraction pattern of the typical σ phase, Co_2V_3 (Figure 4d), which has a tetragonal structure with a space group of $P42/mnm$. Notably, the composition of the σ phase in our Ni–Co–V samples deviate from the chemical stoichiometry of Co_2V_3 , resulting in some ordering diffraction spots (within the yellow circle in Figure 4c) that violate the ideal extinction conditions. Figure 4e displays an enlarged view of the region highlighted in Figure 4a, showing the distribution of σ precipitates within a grain. It can be seen that spherical σ precipitates form along dislocation, revealing a dislocation-assisted precipitation behavior. Moreover, the energy-dispersive X-ray spectroscopy (EDX) mapping (Figure 4f–h) shows these σ precipitates are enriched in V and depleted in Ni and Co.

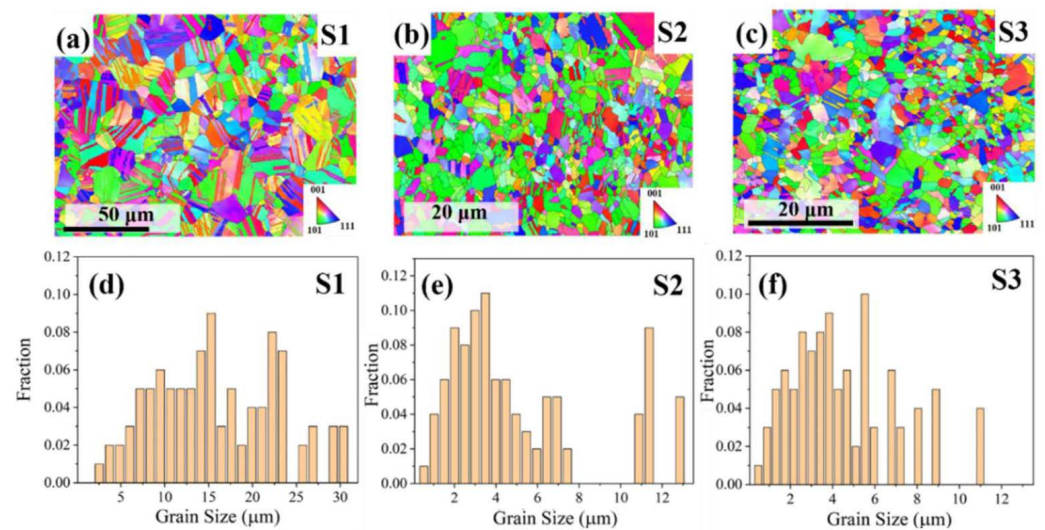


Figure 3. IPFs of recrystallized S1 (a), S2 (b) and S3 (c) samples. Grain size distribution of recrystallized S1 (d), S2 (e) and S3 (f) samples.

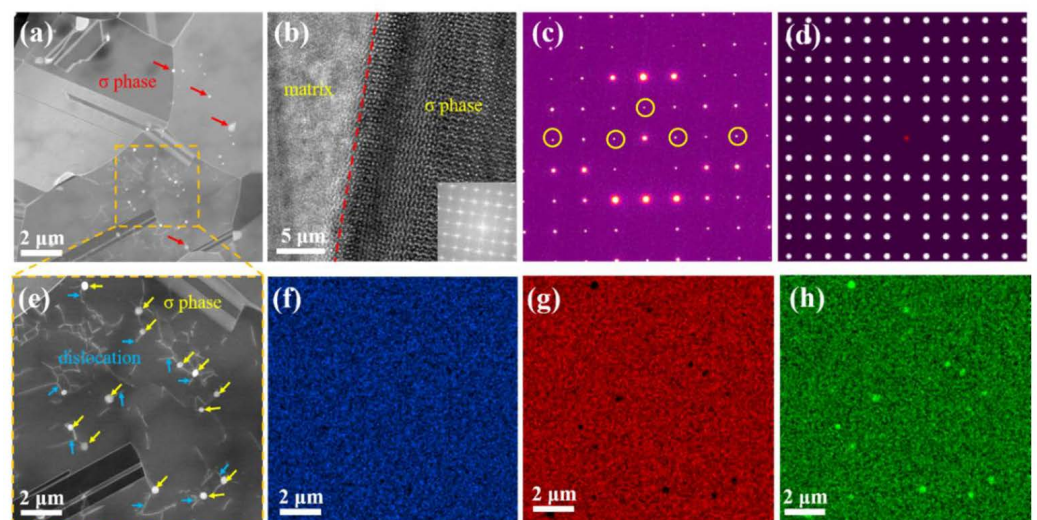


Figure 4. Precipitation behavior in large-grained S1 sample. (a) HAADF image showing spatial distribution of σ precipitates. (b) HRTEM image detailing the interface between matrix and σ precipitate. (c) SAED pattern of σ precipitate along the [001] zone axis, which closely matches the calculated diffraction pattern (d) of a typical σ phase, Co_2V_3 . The yellow circles highlight the violation of the extinction diffraction condition. (e) HAADF image showing dislocation-assisted σ precipitation behavior within grains. (f–h) Elemental distribution of Ni, Co, V in the region shown in (e).

The σ phase in the small-grained samples were also examined. Figure 5a shows a typical spatial distribution of σ precipitates in the small-grained sample. This clearly demonstrates that σ precipitates are predominantly located at grain boundaries, with an average diameter of ~ 455 nm, and some smaller σ precipitates are found within the grains, with an average diameter of ~ 180 nm. Furthermore, some nanoscale annealing twins, with an average width of ~ 306 nm, are formed in these small grains, contrasting with relatively large annealing twins in sample S1 observed by EBSD. These observations demonstrate that a decrease of grain size can reduce the width of annealing twins. The EDX mapping in Figure 5b–d reveals that the white σ spherical particles in Figure 5a are enriched in V and depleted in Ni and Co. A quantitative line scan analysis in Figure 5e reveals the compositional difference between the matrix and σ precipitates.

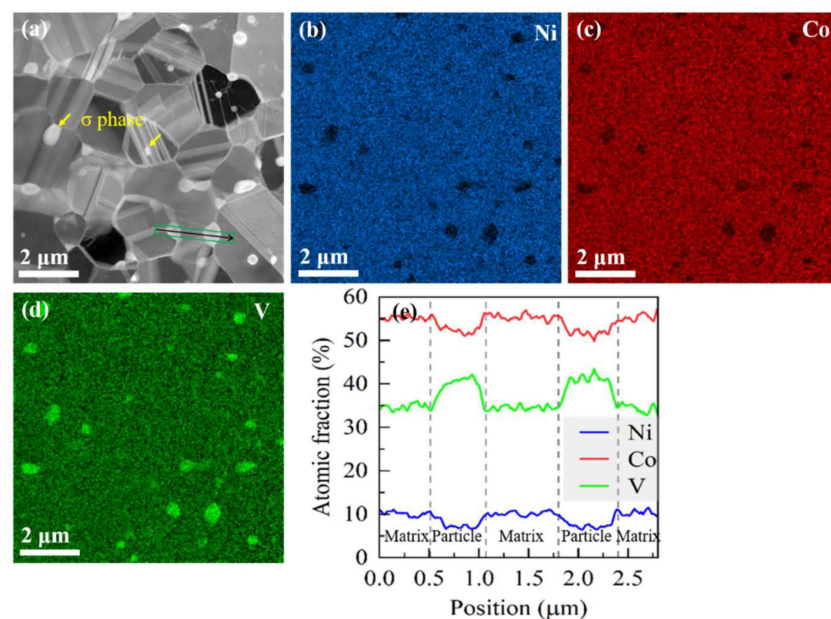


Figure 5. Precipitation behavior in small-grained S3 sample. (a) HAADF image showing spatial distribution of σ precipitates. (b–d) EDX maps of Ni, Co, and V elements in the region shown in (a). (e) Compositional profiles obtained by an EDX line scan along the direction indicated by the black arrow in (a).

3.2. Local Lattice Distortion

DFT calculations were conducted to examine the LLD in the $\text{Ni}_{10}\text{Co}_{56.5}\text{V}_{33.5}$ MPEA. Figure 6a illustrates the stable supercell structure following the relaxation of ionic positions. It is evident that atoms deviate from their ideal lattice positions, indicating the existence of large LLD. We further calculated the statistical distribution of atomic distances among the nearest neighboring atoms in the relaxed supercell, as depicted in Figure 6b. Notably, the distances of V–V atomic pairs significantly exceed those of other atomic pairs, which is consistent with the larger atomic radius of V compared with Ni and Co elements [36]. Therefore, V–V atomic pairs contribute most significantly to the LLD in the Ni–Co–V MPEA. A widely-adopted parameter for quantifying LLD in MPEAs is the size mismatch parameter [37],

$$\delta = \sqrt{\frac{\sum_{i=1}^N c_i \left(1 - r_i / \sum_{j=1}^N c_j r_j\right)^2}{\sum_{i=1}^N c_i}} \quad (1)$$

where N , $c_{i,j}$, and $r_{i,j}$ are the total number of constituent elements, atomic fraction, and atomic radius of the i th or j th element, respectively. Using atomic radii in [38], we calculated the δ (0.059) of our newly-designed $\text{Ni}_{10}\text{Co}_{56.5}\text{V}_{33.5}$ MPEA, which is comparable with the value (0.062) of the equiatomic NiCoV MPEA but is notably larger than that of the most studied damage-tolerant CoCrFeNiMn (0.039) and NiCoCr (0.048) MPEAs.

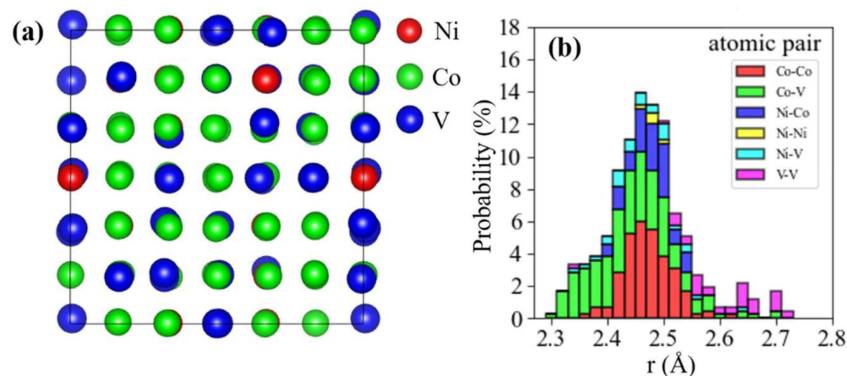


Figure 6. (a) Projection view of the relaxed supercell along [100] orientation. (b) Histogram of atomic pair distances among the first nearest neighboring atoms.

3.3. Mechanical Properties

Figure 7a presents the engineering stress–strain curves obtained from tensile tests conducted at 77 K. As grain size decreases from the S1 sample to S3 sample, both yield strength and tensile strength increase, while elongation decreases. The large-grained S1 sample shows an excellent elongation of 47%, with a moderate yield strength of 841 MPa and a high ultimate tensile strength (UTS) of 1434 MPa. Samples S2 and S3 demonstrate a superior balance between strength and ductility. Specifically, S2 exhibits a yield strength of 1184 MPa and a UTS of 1804 MPa, coupled with an elongation of 33.5%. Conversely, S3 is characterized by a higher yield strength of 1400 MPa and a UTS of 1890 MPa, with a slightly lower elongation of 23%. Figure 7b plots strain hardening rate against true strain, revealing that all samples undergo three stages of strain hardening: a rapid decrease at the beginning of plastic deformation, followed by a swift increase, and then a gradual decline before fracture. The second stage is closely related to the yield stage phenomena, as shown in the inset in Figure 7a.

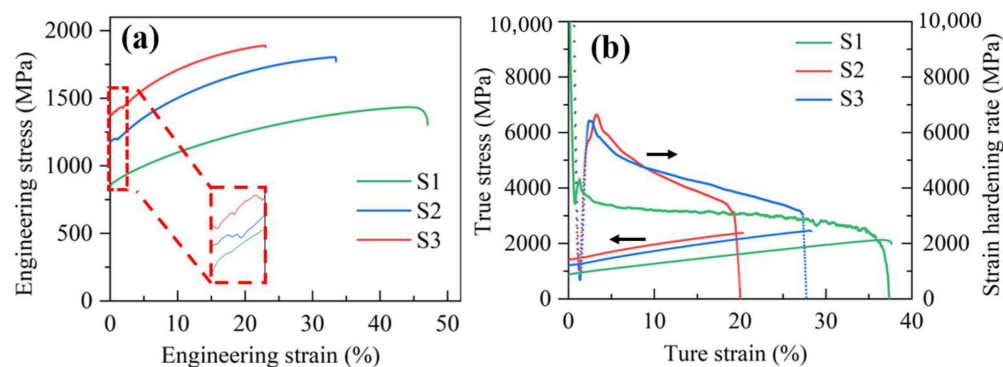


Figure 7. (a) Engineering stress–strain curves. (b) Strain hardening rate vs. true strain. Arrows indicate the y axes of different curves.

Figure 8 plots the product of UTS and elongation against yield strength for various MPEAs measured at 77 K. It can be seen that our newly designed $\text{Ni}_{10}\text{Co}_{56.5}\text{V}_{33.5}$ MPEA exhibits exceptional combination of strength and ductility at 77 K. Compared with the equiatomic NiCoV MPEA, the yield strength of the designed $\text{Ni}_{10}\text{Co}_{56.5}\text{V}_{33.5}$ MPEA increases by 57.8% from 887 MPa to 1400 MPa. The mechanical performance of the $\text{Ni}_{10}\text{Co}_{56.5}\text{V}_{33.5}$ MPEA is better than most of the multiphase MPEAs.

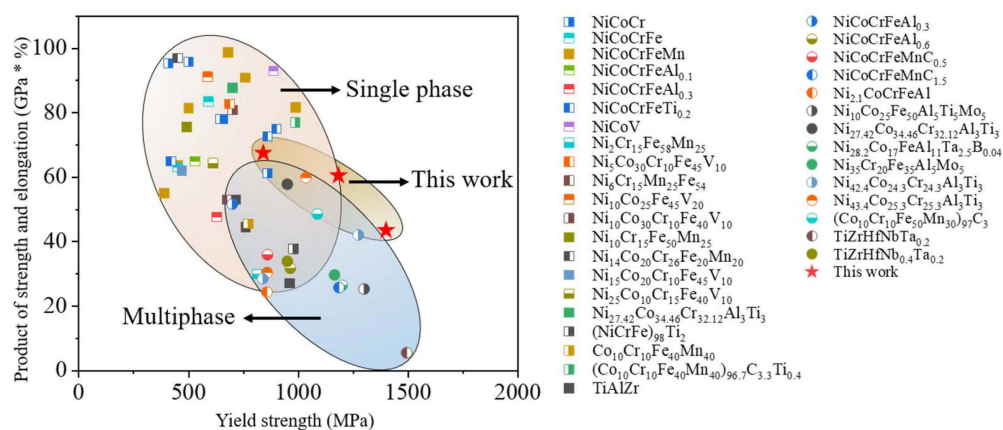


Figure 8. Yield strength vs. product of UTS and elongation of MPEAs at 77 K. The yield strength, ultimate tensile strength, and elongation values of other MPEAs adapted from [8,10–12,27,39–70].

3.4. Fractography

Fractography of the deformed samples was examined using SEM, as shown in Figure 9. A deep dimple structure was observed in the S1 sample. In contrast, the dimples in samples S2 and S3 are rather small and shallow. Compared with samples S2 and S3, the formation of the rougher fracture surface in the S1 sample consumes more energy, leading to a higher ductility. Moreover, the average dimple sizes decrease with the reduction of grain size, aligning with the trend that ductility decreases as grain size diminishes (Figure 7a).

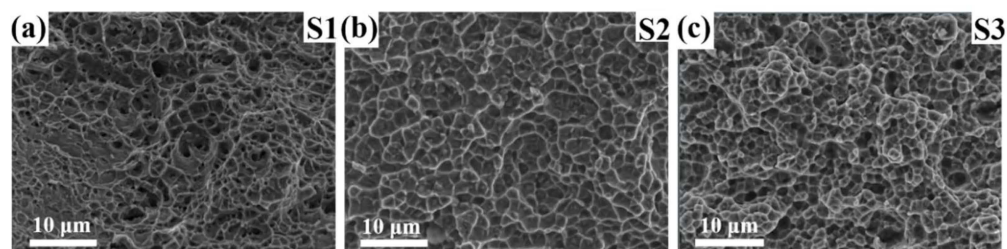


Figure 9. Fractography of the samples deformed at 77 K. Morphology of the fractured surface for sample S1 (a), sample S2 (b), and Sample S3 (c).

4. Discussion

4.1. Grain Size Effect on Deformation Behavior

Figure 10a–c show the Kernal average misorientation (KAM) maps of samples S1 to S3, which generally reflects the density of geometrically necessary dislocations. In the S1 sample, characterized by homogeneous large grains, a high density of dislocations is observed in most grains, indicating cooperative plastic deformation among different grains. For samples S2 and S3, which feature heterogeneous and smaller grains, the density of dislocations dramatically decreases, and dislocation cells, especially in large grains, are formed. Grain reference orientation deviation (GROD) analysis was further conducted to examine large orientation changes within grains caused by deformation, as shown in Figure 10d–f. It is apparent that most grains in the S1 sample underwent severe orientation changes in order to accommodate large plastic deformation, and a large amount of low-angle grain boundaries are formed. In the small-grained S2 and S3 samples, large GROD occurs only within large grains, whereas GROD in small grains remains minimal, demonstrating a heterogeneous plastic deformation behavior.

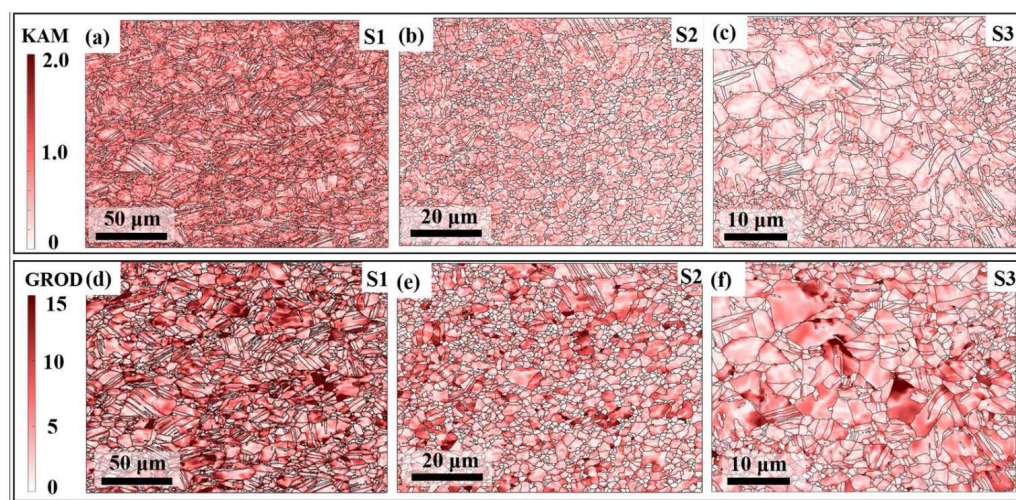


Figure 10. (a–c) KAM maps of fractured samples S1 to S3. The color bar on the left indicates the degree of misorientation. (d–f) GROD maps. The color bar indicates the degree of orientation change within grains.

4.2. Deformation Mechanisms

To investigate the deformation mechanisms, we conducted TEM and PED characterizations on the fractured samples. Figure 11a shows the bright-field TEM image of the fractured S1 sample. We observe the formation of multiple bands with varying width. SAED analysis was also conducted to determine whether these bands are deformation twins. The SAED pattern, shown in the inset of Figure 11a, reveals diffraction spots from only the single FCC phase. This observation indicates that these deformation bands are not deformation twins. Based on their longitudinal orientation, these deformation bands can be classified as the $\langle 001 \rangle$ band or the $\langle \bar{1}11 \rangle$ band. To further confirm the nature of these bands, PED analysis was performed on the region outlined by the blue dashed box in Figure 11a. The IPF map in Figure 11b shows that the normal direction of the matrix plane aligns with the $[110]$ direction, while the normal direction of the bands significantly deviates from the $[110]$ orientation with severe twist angles exceeding 15° relative to the matrix. These bands twist towards either the $\langle 111 \rangle$ or $\langle 100 \rangle$ direction. Further analysis of the orientation differences between these bands and the matrix is presented in Figure 11c, which plots the orientation deviation profiles along three lines in Figure 11b. It is apparent that some deformation bands can rotate at an angle of nearly 60° , close to the angle of deformation twins. Figure 11d shows a typical HRTEM image of the interface between the matrix and deformation band. This further proves that the deformation band is not a deformation twin, and that the inset FFT pattern reveals that the deformation band greatly twisted away from the $[110]$ normal direction of the matrix. These deformation bands demonstrate that dislocations within these bands can cooperatively rotate to accommodate large plastic deformation.

In addition to deformation bands, the fractured S1 sample also exhibited other deformation mechanisms, such as SFs and deformation twins. The bright-field TEM image (Figure 12a) demonstrates intersecting SFs within a grain, characterized by multiple deformation bands in the matrix. The magnified view in Figure 12b reveals a network of interwoven SFs, segmenting the matrix into nanoscale subdivisions. Moreover, nanoscale deformation twins, observed sporadically, serve as barriers to hinder the propagation of SFs, as shown in the HRTEM image (Figure 12c). In grains lacking severely distorted deformation bands, an extensive formation of SFs during plastic deformation is noted, as illustrated in Figure 12d. A SAED pattern from Figure 12d, taken along the $[110]$ zone axis, discloses characteristic streaking along two directions, signifying the presence of SFs. Figure 12e zooms into the area highlighted by the orange dashed line in Figure 12d, exposing a hierarchical organization of primary and secondary SFs. This arrangement further

subdivides the grains into nanoscale regions, invoking a dynamic Hall–Petch effect. Lastly, an HRTEM image in Figure 12f sheds light on the intricate interactions between SFs along two orientations. It is evident that SFs on different $\{111\}$ slip planes intersect, creating characteristic sessile Lomer–Cottrell (LC) locks that potentially obstruct dislocation movement.

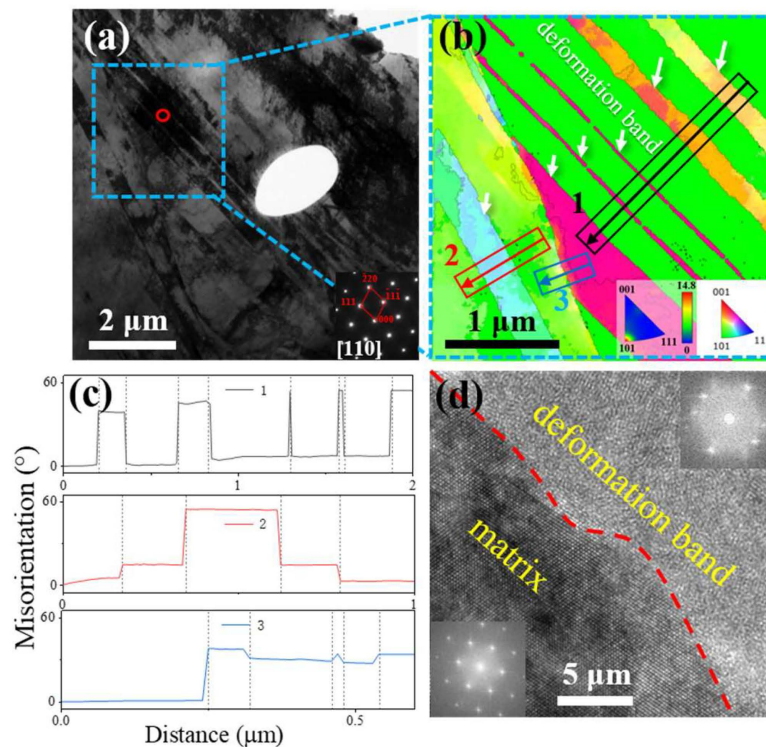


Figure 11. (a) Bright-field TEM image showing deformation bands in the large-grained S1 sample. The inset displays the SAED pattern along the $[110]$ direction of the region highlighted by the red circle. (b) PED result showing the grain orientation change induced by deformation bands. (c) Orientation change profiles for the 1, 2, 3 directions indicated in (b). (d) HRTEM image showing the interface between the matrix and the deformation band. Insets show the corresponding FFT patterns of the matrix and deformation band.

Further analysis focused on the deformation mechanisms within small-grained samples. Figure 13a presents an ABF–STEM image capturing the characteristic deformation microstructure of the fractured S3 sample. Notably, a high density of straight SFs, aligned in a singular direction and forming channels approximately 50 nm wide across each grain. These channels, formed by SFs, effectively confine dislocation movement within them (Figure 13b), thereby providing a dynamic Hall–Petch strengthening mechanism. Consistent with the dynamic Hall–Petch strengthening, the inverse fast Fourier transform (IFFT) of the HRTEM image (inset of Figure 13c) shows a substantial accumulation of dislocations on both sides of the SF, which contributes to the channel formation. The presence of streaking perpendicular to the SFs in the inset of Figure 13a further confirms that the straight lines in Figure 13a are indeed SFs. The presence of SFs in the $\text{Ni}_{10}\text{Co}_{56.5}\text{V}_{33.5}$ MPEA suggests a low SFE; however, contrary to expectations of planar slip, wavy dislocations predominate, as depicted in Figure 13b. In this way, the dislocation morphology aligns with the large LLD characteristic of the $\text{Ni}_{10}\text{Co}_{56.5}\text{V}_{33.5}$ MPEA. Additionally, deformation bands were detected in the small-grained S3 sample, as revealed in the bright-field TEM image (Figure 13d), with dense dislocations constrained within these deformation bands. The HAADF image of the same area (Figure 13e) reveals that the dense SFs, interspersed throughout both the matrix and the deformation bands exhibit varied orientations. This orientation discrepancy suggests that the deformation bands are markedly twisted, with

band boundaries serving as effective impediments to the further spread of SFs within the matrix, thereby contributing to the strengthening effect.

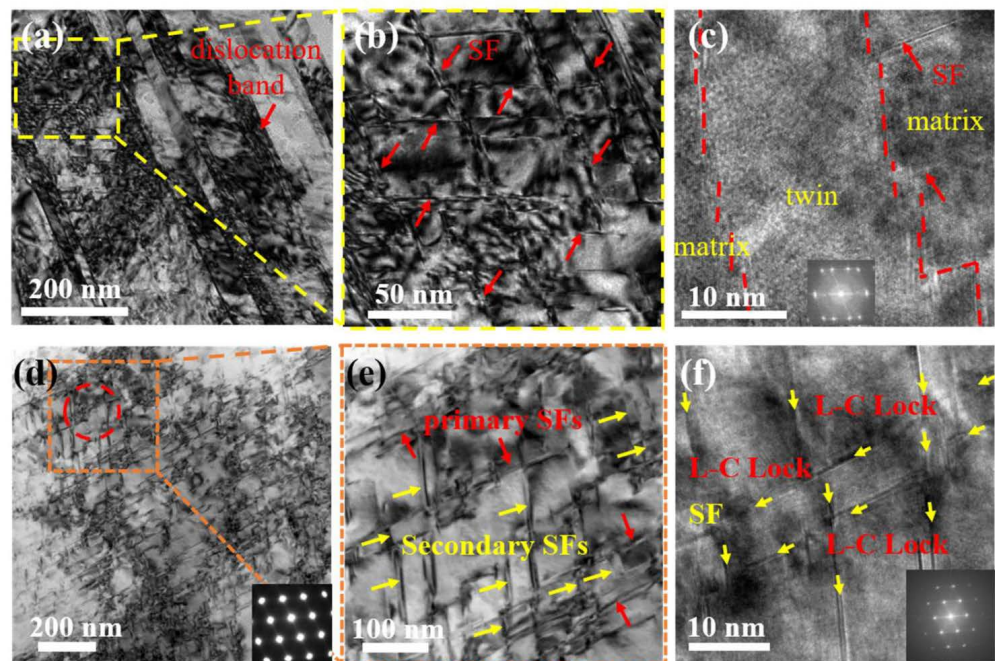


Figure 12. (a) Bright-field TEM image showing dislocation bands and SFs in the fractured S1 sample. (b) An enlarged view of the area enclosed by the yellow dashed line in (a). (c) HRTEM image of the interaction between the deformation twin and SFs, with the inset showing the FFT pattern of the deformation twin. (d) Annular bright-field scanning TEM (ABF-STEM) image showing SFs. The inset displays the SAED pattern of the region highlighted by the red dashed line. (e) A magnified view of the region in orange dashed box in (d). (f) HRTEM image of Lomer–Cottrell locks formed by SFs.

Our study on deformation mechanisms has revealed that SFs and dislocations serve as the primary mechanisms across both large- and small-grained samples. Furthermore, the abundant formation of SFs and deformation bands in both large- and small-grained samples acts as an effective barrier to dislocation movement, thereby contributing to the MPEA's enhanced strength. A distinctive feature of the deformation mechanism in our newly designed MPEA is the emergence of severely twisted dislocation bands. Similar dislocation bands or microbands have been identified in alloys such as Fe–28Mn–9Al–0.8C steel [71], Inconel 718 [72], and NiCoFe-based MPEA [73], where these alloys typically exhibit relatively low SFE, conducive to the formation of coplanar dislocations. However, the $\text{Ni}_{10}\text{Co}_{56.5}\text{V}_{33.5}$ MPEA distinguishes itself through the development of exceptionally twisted deformation bands, facilitating a more effective accommodation of large plastic deformation. While the SFE of the $\text{Ni}_{10}\text{Co}_{56.5}\text{V}_{33.5}$ is low enough to enable the formation of SFs and deformation twins, coplanar dislocations are not prevalent within this MPEA. Instead, the wavy dislocation morphology observed in the $\text{Ni}_{10}\text{Co}_{56.5}\text{V}_{33.5}$ MPEA aligns with the substantial LLD, offering a strong drag effect on dislocation motion, thus enhancing the alloy's strength. Admittedly, the high strength of the $\text{Ni}_{10}\text{Co}_{56.5}\text{V}_{33.5}$ MPEA also stems from precipitate strengthening and strengthening from dislocations that are initially stored in recrystallized samples. The impact of these factors, however, is limited due to their low proportion of precipitates and dislocations.

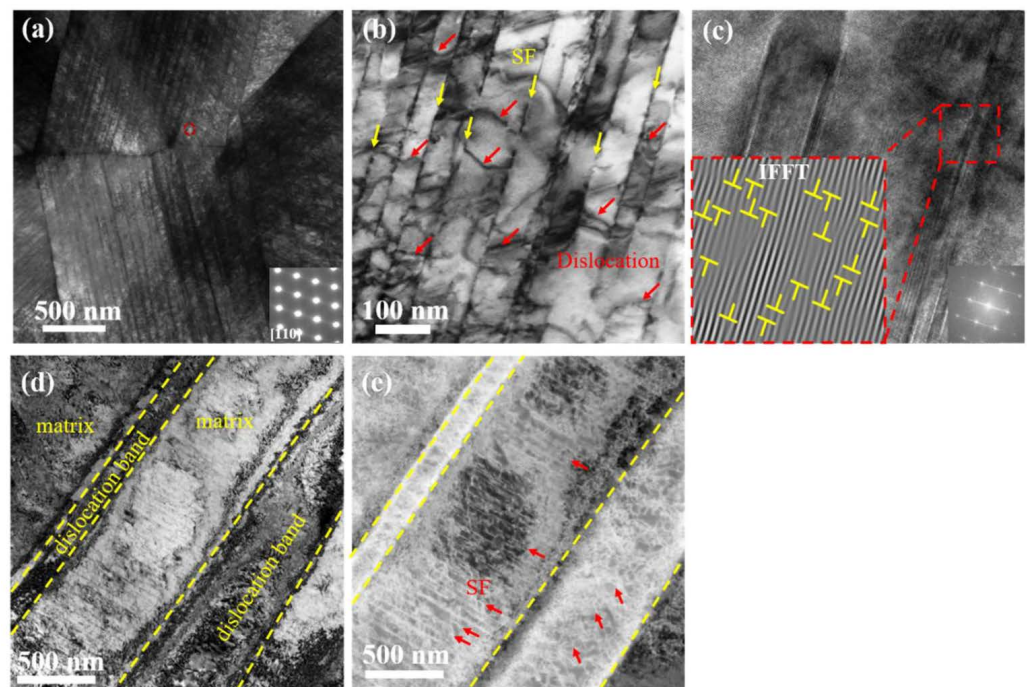


Figure 13. (a) ABF-STEM image of the fractured small-grained S3 sample. The inset diffraction pattern was taken from the region highlighted by red circle. (b) A magnified ABF-STEM image showing the interaction of SFs and dislocations. (c) HRTEM image of the SF region, with the inset showing the IFFT-magnified image enclosed by a red dashed line. Yellow T-shapes marks highlight edge dislocations. (d) Bright-field TEM image of deformation bands. (e) HAADF image of SFs with different orientations in the matrix and deformation band.

5. Conclusions

In summary, we have designed a non-equiatomic $\text{Ni}_{10}\text{Co}_{56.5}\text{V}_{33.5}$ MPEA that exhibits a superior balance between strength and ductility at the cryogenic temperature of 77 K, achieved by optimizing LLD and SFE. The microstructure and deformation mechanisms were carefully characterized by HEXRD, EBSD, TEM, and PED. The DFT calculations provided the fundamental understandings of the LLD. Based on our observations, some key conclusions can be drawn, as follows:

- In the developed $\text{Ni}_{10}\text{Co}_{56.5}\text{V}_{33.5}$ MPEA, the predominant phase is FCC accompanied by a minor σ phase, the latter constituting less than 3.0% by volume. In samples with larger grains, precipitates primarily form along dislocations within the grains, whereas in those with smaller grains, precipitates are predominantly formed at grain boundaries.
- After recrystallization heat treatments, the large-grained sample shows a relatively uniform grain size, while the small-grained sample exhibits a heterogeneous microstructure composed of both large and small grains.
- DFT calculations reveal pronounced LLD in the $\text{Ni}_{10}\text{Co}_{56.5}\text{V}_{33.5}$ MPEA, as atoms deviate from ideal lattice sites, with V-V atomic pairs showing the greatest distances due to vanadium's larger atomic size. The size mismatch parameter calculated for this MPEA is comparable with the value for the equiatomic NiCoV MPEA.
- By tuning the grain size, the $\text{Ni}_{10}\text{Co}_{56.5}\text{V}_{33.5}$ MPEA exhibits a yield strength ranging from 841 to 1400 MPa and an ultimate tensile strength from 1434 to 1890 MPa, with ductility ranging from 47% to 23%.
- In the large-grained sample, the primary deformation mechanisms encompass severely twisted deformation bands exhibiting rotation angles nearing 60° , hierarchical SFs, and sporadic deformation twins. Conversely, the small-grained sample displays a deformation microstructure defined by deformation bands and SFs aligned in one

direction within each grain. The formation of dislocation bands and SFs contributes to a dynamic Hall–Petch effect.

Thus, our study offers insights into the design of strong and ductile MPEAs for applications at cryogenic temperatures by optimizing LLD and SFE. On the other hand, the new deformation mechanism of severely distorted deformation band found in the Ni₁₀Co_{56.5}V_{33.5} MPEA needs further study to understand its origin.

Author Contributions: Conceptualization, Y.T. and W.L.; methodology, Y.T. and C.S.; formal analysis, D.Z., C.S., W.L. and Y.T.; investigation, D.Z., C.W., R.S. and Y.T.; resources, Y.T.; data curation, D.Z. and Y.T.; writing—original draft, D.Z. and Y.T., writing—review and editing, Y.T., C.S. and W.L. All authors have read and agreed to the published version of the manuscript.

Funding: Y.T. gratefully acknowledges the financial support of the National Natural Science Foundation of China (Grant No. 52371164), the Taishan Scholars Program of Shandong Province (tsqn202103052), and the Yantai city matching fund for Taishan Scholars Program of Shandong Province.

Data Availability Statement: The raw data supporting the conclusions of this article will be made available by the authors on request.

Acknowledgments: AI tool: ChatGPT4, was utilized solely for grammar and syntax checking in the manuscript.

Conflicts of Interest: The authors declare no conflict of interest.

References

1. Cantor, B.; Chang, I.T.H.; Knight, P.; Vincent, A.J.B. Microstructural development in equiatomic multicomponent alloys. *Mater. Sci. Eng. A* **2004**, *375–377*, 213–218. [[CrossRef](#)]
2. Yeh, J.W.; Chen, S.K.; Lin, S.J.; Gan, J.Y.; Chin, T.S.; Shun, T.T.; Tsau, C.H.; Chang, S.Y. Nanostructured High-Entropy Alloys with Multiple Principal Elements: Novel Alloy Design Concepts and Outcomes. *Adv. Eng. Mater.* **2004**, *6*, 299–303. [[CrossRef](#)]
3. Zhang, Y.; Zuo, T.T.; Tang, Z.; Gao, M.C.; Dahmen, K.A.; Liaw, P.K.; Lu, Z.P. Microstructures and properties of high-entropy alloys. *Prog. Mater. Sci.* **2014**, *61*, 1–93. [[CrossRef](#)]
4. Miracle, D.B.; Senkov, O.N. A critical review of high entropy alloys and related concepts. *Acta Mater.* **2017**, *122*, 448–511. [[CrossRef](#)]
5. George, E.P.; Raabe, D.; Ritchie, R.O. High-entropy alloys. *Nat. Rev. Mater.* **2019**, *4*, 515–534. [[CrossRef](#)]
6. Ye, Y.F.; Wang, Q.; Lu, J.; Liu, C.T.; Yang, Y. High-entropy alloy: Challenges and prospects. *Mater. Today* **2016**, *19*, 349–362. [[CrossRef](#)]
7. Senkov, O.N.; Wilks, G.B.; Scott, J.M.; Miracle, D.B. Mechanical properties of Nb₂₅Mo₂₅Ta₂₅W₂₅ and V₂₀Nb₂₀Mo₂₀Ta₂₀W₂₀ refractory high entropy alloys. *Intermetallics* **2011**, *19*, 698–706. [[CrossRef](#)]
8. Gludovatz, B.; Hohenwarter, A.; Catoor, D.; Chang, E.H.; George, E.P.; Ritchie, R.O. A fracture-resistant high-entropy alloy for cryogenic applications. *Science* **2014**, *345*, 1153–1158. [[CrossRef](#)]
9. Liu, D.; Yu, Q.; Kabra, S.; Jiang, M.; Forna-Kreutzer, P.; Zhang, R.; Payne, M.; Walsh, F.; Gludovatz, B.; Asta, M.; et al. Exceptional fracture toughness of CrCoNi-based medium- and high-entropy alloys at 20 kelvin. *Science* **2022**, *378*, 978–983. [[CrossRef](#)]
10. Zhang, C.; Yu, Q.; Tang, Y.T.; Xu, M.; Wang, H.; Zhu, C.; Ell, J.; Zhao, S.; MacDonald, B.E.; Cao, P.; et al. Strong and ductile FeNiCoAl-based high-entropy alloys for cryogenic to elevated temperature multifunctional applications. *Acta Mater.* **2023**, *242*, 118449. [[CrossRef](#)]
11. Sun, S.J.; Tian, Y.Z.; An, X.H.; Lin, H.R.; Wang, J.W.; Zhang, Z.F. Ultrahigh cryogenic strength and exceptional ductility in ultrafine-grained CoCrFeMnNi high-entropy alloy with fully recrystallized structure. *Mater. Today Nano* **2018**, *4*, 46–53. [[CrossRef](#)]
12. Han, Z.; Ding, C.; Liu, G.; Yang, J.; Du, Y.; Wei, R.; Chen, Y.; Zhang, G. Analysis of deformation behavior of VCoNi medium-entropy alloy at temperatures ranging from 77 K to 573 K. *Intermetallics* **2021**, *132*, 107126. [[CrossRef](#)]
13. Byun, T.S.; Hashimoto, N.; Farrell, K. Temperature dependence of strain hardening and plastic instability behaviors in austenitic stainless steels. *Acta Mater.* **2004**, *52*, 3889–3899. [[CrossRef](#)]
14. Umezawa, O. Review of the Mechanical Properties of High-Strength Alloys at Cryogenic Temperatures. *Mater. Perform. Charact.* **2021**, *10*, 20200138. [[CrossRef](#)]
15. Sohn, S.S.; Kwiatkowski da Silva, A.; Ikeda, Y.; Körmann, F.; Lu, W.; Choi, W.S.; Gault, B.; Ponge, D.; Neugebauer, J.; Raabe, D. Ultrastrong Medium-Entropy Single-Phase Alloys Designed via Severe Lattice Distortion. *Adv. Mater.* **2019**, *31*, 1807142. [[CrossRef](#)] [[PubMed](#)]
16. Lee, C.; Chou, Y.; Kim, G.; Gao, M.C.; An, K.; Brechtel, J.; Zhang, C.; Chen, W.; Poplawsky, J.D.; Song, G.; et al. Lattice-Distortion-Enhanced Yield Strength in a Refractory High-Entropy Alloy. *Adv. Mater.* **2020**, *32*, 2004029. [[CrossRef](#)] [[PubMed](#)]
17. Li, Z.; Ma, S.; Zhao, S.; Zhang, W.; Peng, F.; Li, Q.; Yang, T.; Wu, C.-Y.; Wei, D.; Chou, Y.-C.; et al. Achieving superb strength in single-phase FCC alloys via maximizing volume misfit. *Mater. Today* **2023**, *63*, 108–119. [[CrossRef](#)]

18. Lee, C.; Song, G.; Gao, M.C.; Feng, R.; Chen, P.; Brechtel, J.; Chen, Y.; An, K.; Guo, W.; Poplawsky, J.D.; et al. Lattice distortion in a strong and ductile refractory high-entropy alloy. *Acta Mater.* **2018**, *160*, 158–172. [[CrossRef](#)]
19. Tong, Y.; Zhao, S.; Bei, H.; Egami, T.; Zhang, Y.; Zhang, F. Severe local lattice distortion in Zr- and/or Hf-containing refractory multi-principal element alloys. *Acta Mater.* **2020**, *183*, 172–181. [[CrossRef](#)]
20. Okamoto, N.L.; Yuge, K.; Tanaka, K.; Inui, H.; George, E.P. Atomic displacement in the CrMnFeCoNi high-entropy alloy—A scaling factor to predict solid solution strengthening. *AIP Adv.* **2016**, *6*, 125008. [[CrossRef](#)]
21. Varvenne, C.; Luque, A.; Curtin, W.A. Theory of strengthening in fcc high entropy alloys. *Acta Mater.* **2016**, *118*, 164–176. [[CrossRef](#)]
22. Li, Z.; Pradeep, K.G.; Deng, Y.; Raabe, D.; Tسان, C.C. Metastable high-entropy dual-phase alloys overcome the strength–ductility trade-off. *Nature* **2016**, *534*, 227–230. [[CrossRef](#)] [[PubMed](#)]
23. Zhang, Z.J.; Mao, M.M.; Wang, J.; Gludovatz, B.; Zhang, Z.; Mao, S.X.; George, E.P.; Yu, Q.; Ritchie, R.O. Nanoscale origins of the damage tolerance of the high-entropy alloy CrMnFeCoNi. *Nat. Commun.* **2015**, *6*, 10143. [[CrossRef](#)] [[PubMed](#)]
24. Ming, K.; Lu, W.; Li, Z.; Bi, X.; Wang, J. Amorphous Bands Induced by Low Temperature Tension in a Non-Equiatomic CrMnFeCoNi Alloy. *Acta Mater.* **2020**, *188*, 354–365. [[CrossRef](#)]
25. Li, D.; Liaw, P.K.; Xie, L.; Zhang, Y.; Wang, W. Advanced high-entropy alloys breaking the property limits of current materials. *J. Mater. Sci. Technol.* **2024**, *186*, 219–230. [[CrossRef](#)]
26. George, E.P.; Curtin, W.A.; Tسان, C.C. High entropy alloys: A focused review of mechanical properties and deformation mechanisms. *Acta Mater.* **2020**, *188*, 435–474. [[CrossRef](#)]
27. Miao, J.; Slone, C.E.; Smith, T.M.; Niu, C.; Bei, H.; Ghazisaeidi, M.; Pharr, G.M.; Mills, M.J. The evolution of the deformation substructure in a Ni-Co-Cr equiatomic solid solution alloy. *Acta Mater.* **2017**, *132*, 35–48. [[CrossRef](#)]
28. Yang, D.C.; Jo, Y.H.; Ikeda, Y.; Körmann, F.; Sohn, S.S. Effects of cryogenic temperature on tensile and impact properties in a medium-entropy VCoNi alloy. *J. Mater. Sci. Technol.* **2021**, *90*, 159–167. [[CrossRef](#)]
29. Kresse, G.; Furthmüller, J. Efficiency of ab-initio total energy calculations for metals and semiconductors using a plane-wave basis set. *Comput. Mater. Sci.* **1996**, *6*, 15–50. [[CrossRef](#)]
30. Blöchl, P.E. Projector augmented-wave method. *Phys. Rev. B* **1994**, *50*, 17953–17979. [[CrossRef](#)]
31. Perdew, J.P.; Burke, K.; Ernzerhof, M. Generalized Gradient Approximation Made Simple. *Phys. Rev. Lett.* **1996**, *77*, 3865–3868. [[CrossRef](#)] [[PubMed](#)]
32. Zunger, A.; Wei, S.H.; Ferreira, L.G.; Bernard, J.E. Special quasirandom structures. *Phys. Rev. Lett.* **1990**, *65*, 353–356. [[CrossRef](#)] [[PubMed](#)]
33. Oh, H.; Kim, S.; Odbadrakh, K.; Ryu, W.; Yoon, K.; Mu, S.; Körmann, F.; Ikeda, Y.; Tسان, C.; Raabe, D.; et al. Engineering atomic-level complexity in high-entropy and complex concentrated alloys. *Nat. Commun.* **2019**, *10*, 1234567890. [[CrossRef](#)] [[PubMed](#)]
34. Dodaran, M.S.; Guo, S.; Khonsari, M.M.; Shamsaei, N.; Shao, S. A theoretical calculation of stacking fault energy of Ni alloys: The effects of temperature and composition. *Comput. Mater. Sci.* **2021**, *191*, 110326. [[CrossRef](#)]
35. Choi, W.; Jo, Y.H.; Kim, D.G.; Sohn, S.S.; Lee, S.; Lee, B. A thermodynamic description of the Co-Cr-Fe-Ni-V system for high-entropy alloy design. *Calphad* **2019**, *66*, 101624. [[CrossRef](#)]
36. Yin, B.; Maresca, F.; Curtin, W.A. Vanadium is an optimal element for strengthening in both fcc and bcc high-entropy alloys. *Acta Mater.* **2020**, *188*, 486–491. [[CrossRef](#)]
37. Zhang, Y.; Zhou, Y.J.; Lin, J.P.; Chen, G.L.; Liaw, P.K. Solid-Solution Phase Formation Rules for Multi-component Alloys. *Adv. Eng. Mater.* **2008**, *10*, 534–538. [[CrossRef](#)]
38. Periodictable. Available online: <https://periodictable.com/> (accessed on 4 April 2024).
39. Han, B.; Zhang, C.; Feng, K.; Li, Z.; Zhang, X.; Shen, Y.; Wang, X.; Kokawa, H.; Li, R.; Wang, Z.; et al. Additively manufactured high strength and ductility CrCoNi medium entropy alloy with hierarchical microstructure. *Mater. Sci. Eng. A* **2021**, *820*, 141545. [[CrossRef](#)]
40. Wu, Z.; Bei, H.; Pharr, G.M.; George, E.P. Temperature dependence of the mechanical properties of equiatomic solid solution alloys with face-centered cubic crystal structures. *Acta Mater.* **2014**, *81*, 428–441. [[CrossRef](#)]
41. Gludovatz, B.; Hohenwarter, A.; Thurston, K.V.; Bei, H.; Wu, Z.; George, E.P.; Ritchie, R.O. Exceptional damage-tolerance of a medium-entropy alloy CrCoNi at cryogenic temperatures. *Nat. Commun.* **2016**, *7*, 10602. [[CrossRef](#)]
42. Li, J.; Xiao, L.; Ma, X.; Lu, K.; Li, F.; Chen, J. Achieving ultrahigh cryogenic yield strength and sufficient ductility in a medium-entropy alloy via bimodal grain design. *Mater. Sci. Eng. A* **2023**, *863*, 144491. [[CrossRef](#)]
43. Liu, J.; Guo, X.; Lin, Q.; He, Z.; An, X.; Li, L.; Liaw, P.K.; Liao, X.; Yu, L.; Lin, J.; et al. Excellent ductility and serration feature of metastable CoCrFeNi high-entropy alloy at extremely low temperatures. *Sci. China Mater.* **2019**, *62*, 853–863. [[CrossRef](#)]
44. Kireeva, I.V.; Chumlyakov, Y.I.; Vyrodova, A.V.; Pobedennaya, Z.V.; Karaman, I. Effect of twinning on the orientation dependence of mechanical behaviour and fracture in single crystals of the equiatomic CoCrFeMnNi high-entropy alloy at 77K. *Mater. Sci. Eng. A* **2020**, *784*, 139315. [[CrossRef](#)]
45. Laplanche, G.; Kostka, A.; Horst, O.M.; Eggeler, G.; George, E.P. Microstructure evolution and critical stress for twinning in the CrMnFeCoNi high-entropy alloy. *Acta Mater.* **2016**, *118*, 152–163. [[CrossRef](#)]
46. Seol, J.B.; Bae, J.W.; Kim, J.G.; Sung, H.; Li, Z.; Lee, H.H.; Shim, S.H.; Jang, J.H.; Ko, W.-S.; Hong, S.I.; et al. Short-range order strengthening in boron-doped high-entropy alloys for cryogenic applications. *Acta Mater.* **2020**, *194*, 366–377. [[CrossRef](#)]

47. Kim, Y.-K.; Lee, K.-A. Influence of carbon contents on the cryogenic mechanical properties of precipitation-hardened CrMnFeCoNi high-entropy alloys manufactured by laser powder bed fusion. *Mater. Sci. Eng. A* **2023**, *873*, 145042. [[CrossRef](#)]
48. Li, J.; Lu, K.; Wang, Y.; Zhang, Y.; Ma, X.; Chen, J.; Zhu, Y. Exceptional cryogenic strength and sufficient ductility of a nanotwinned high-entropy alloy fabricated by cryogenic multi-directional compression. *J. Alloys Compd.* **2023**, *931*, 167533. [[CrossRef](#)]
49. Kireeva, I.V.; Chumlyakov, Y.I.; Pobedennaya, Z.V.; Vyrodova, A.V.; Kuksgauzen, I.V.; Kuksgauzen, D.A. Orientation and temperature dependence of a planar slip and twinning in single crystals of Al_{0.3}CoCrFeNi high-entropy alloy. *Mater. Sci. Eng. A* **2018**, *737*, 47–60. [[CrossRef](#)]
50. Kireeva, I.V.; Chumlyakov, Y.I.; Pobedennaya, Z.V.; Vyrodova, A.V. Effect of γ' -phase particles on the orientation and temperature dependence of the mechanical behaviour of Al_{0.3}CoCrFeNi high-entropy alloy single crystals. *Mater. Sci. Eng. A* **2020**, *772*, 138772. [[CrossRef](#)]
51. Li, Q.; Zhang, T.W.; Qiao, J.W.; Ma, S.G.; Zhao, D.; Lu, P.; Wang, Z.H. Mechanical properties and deformation behavior of dual-phase Al_{0.6}CoCrFeNi high-entropy alloys with heterogeneous structure at room and cryogenic temperatures. *J. Alloys Compd.* **2020**, *816*, 152663. [[CrossRef](#)]
52. Yuan, J.; Zhang, H.; Wang, Z.; Han, P.; Qiao, J. Contribution of coherent precipitates on mechanical properties of CoCrFeNiTi_{0.2} high-entropy alloy at room and cryogenic temperatures. *Intermetallics* **2023**, *154*, 107820. [[CrossRef](#)]
53. Tong, Y.; Chen, D.; Han, B.; Wang, J.; Feng, R.; Yang, T.; Zhao, C.; Zhao, Y.L.; Guo, W.; Shimizu, Y.; et al. Outstanding tensile properties of a precipitation-strengthened FeCoNiCrTi_{0.2} high-entropy alloy at room and cryogenic temperatures. *Acta Mater.* **2019**, *165*, 228–240. [[CrossRef](#)]
54. Bhattacharjee, T.; Zheng, R.; Chong, Y.; Sheikh, S.; Guo, S.; Clark, I.T.; Okawa, T.; Wani, I.S.; Bhattacharjee, P.P.; Shibata, A.; et al. Effect of low temperature on tensile properties of AlCoCrFeNi_{2.1} eutectic high entropy alloy. *Mater. Chem. Phys.* **2018**, *210*, 207–212. [[CrossRef](#)]
55. Jo, Y.H.; Yang, J.; Doh, K.-Y.; An, W.; Kim, D.W.; Sung, H.; Lee, D.; Kim, H.S.; Sohn, S.S.; Lee, S. Analysis of damage-tolerance of TRIP-assisted V₁₀Cr₁₀Fe₄₅Co₃₀Ni₅ high-entropy alloy at room and cryogenic temperatures. *J. Alloys Compd.* **2020**, *844*, 156090. [[CrossRef](#)]
56. Gao, X.; Jiang, W.; Lu, Y.; Ding, Z.; Liu, J.; Liu, W.; Sha, G.; Wang, T.; Li, T.; Chang, I.T.H.; et al. Excellent strength-ductility combination of Cr₂₆Mn₂₀Fe₂₀Co₂₀Ni₁₄ high-entropy alloy at cryogenic temperatures. *J. Mater. Sci. Technol.* **2023**, *154*, 166–177. [[CrossRef](#)]
57. Jo, Y.H.; Doh, K.-Y.; Kim, D.G.; Lee, K.; Kim, D.W.; Sung, H.; Sohn, S.S.; Lee, D.; Kim, H.S.; Lee, B.-J.; et al. Cryogenic-temperature fracture toughness analysis of non-equi-atomic V₁₀Cr₁₀Fe₄₅Co₂₀Ni₁₅ high-entropy alloy. *J. Alloys Compd.* **2019**, *809*, 151864. [[CrossRef](#)]
58. Jang, M.J.; Kwak, H.; Lee, Y.W.; Jeong, Y.; Choi, J.; Jo, Y.H.; Choi, W.-M.; Sung, H.J.; Yoon, E.Y.; Praveen, S.; et al. Plastic Deformation Behavior of 40Fe–25Ni–15Cr–10Co–10V High-Entropy Alloy for Cryogenic Applications. *Met. Mater. Int.* **2019**, *25*, 277–284. [[CrossRef](#)]
59. Zhang, Z.; Wang, W.; Qin, S.; Yang, M.; Wang, J.; Jiang, P.; Yuan, F.; Wu, X. Dual heterogeneous structured medium-entropy alloys showing a superior strength-ductility synergy at cryogenic temperature. *J. Mater. Res. Technol.* **2022**, *17*, 3262–3276. [[CrossRef](#)]
60. Peng, H.; Huang, S.; Hu, L.; Luo, B.; Li, L.; Baker, I. Electron beam welding of L12-nanoparticle-strengthened strong and ductile medium-entropy alloys for cryogenic applications. *Mater. Sci. Eng. A* **2024**, *889*, 145875. [[CrossRef](#)]
61. Li, Y.X.; Nutor, R.K.; Zhao, Q.K.; Zhang, X.P.; Cao, Q.P.; Sohn, S.S.; Wang, X.D.; Ding, S.Q.; Zhang, D.X.; Zhou, H.F.; et al. Unraveling the deformation behavior of the Fe₄₅Co₂₅Ni₁₀V₂₀ high entropy alloy. *Int. J. Plast.* **2023**, *165*, 103619. [[CrossRef](#)]
62. Kwon, H.; Sathiyamoorthi, P.; Karthik, G.M.; Asghari-Rad, P.; Zargarani, A.; Do, H.-S.; Lee, B.-J.; Kato, H.; Kim, H.S. 2.3 GPa cryogenic strength through thermal-induced and deformation-induced body-centered cubic martensite in a novel ferrous medium entropy alloy. *Scr. Mater.* **2021**, *204*, 114157. [[CrossRef](#)]
63. Wang, H.; Zhang, K.; Chen, L.; Gao, Q.; Zhao, X.; Chen, C.; Han, Z.; Wei, R. Strengthening Fe_{50+x}Mn₂₅Cr₁₅Ni_{10-x} medium-entropy alloys by Ni/Fe replacement: Experiments and molecular dynamics study. *Intermetallics* **2023**, *155*, 107833. [[CrossRef](#)]
64. Yin, Y.; Tan, Q.; Yang, N.; Chen, X.; Ren, W.; Liu, L.; Chen, H.; Atrens, A.; Ma, N.; Huang, H.; et al. Cost-effective and facile route to ultrafine-microstructure high-entropy alloy for cryogenic applications. *Mater. Sci. Eng. A* **2023**, *881*, 145408. [[CrossRef](#)]
65. Wang, H.; Sun, Q.Y.; Xiao, L.; Sun, J. Effect of grain size on twinning behavior in Ti–2Al–2.5Zr alloy fatigued at 77K. *Mater. Sci. Eng. A* **2012**, *542*, 1–7. [[CrossRef](#)]
66. Wen, X.; Zhu, L.; Naem, M.; Huang, H.; Jiang, S.; Wang, H.; Liu, X.; Zhang, X.; Wang, X.-L.; Wu, Y.; et al. Strong work-hardenable body-centered-cubic high-entropy alloys at cryogenic temperature. *Scr. Mater.* **2023**, *231*, 115434. [[CrossRef](#)]
67. Ma, D.; Xu, H.; Ding, J.; Shen, Y.; Zhang, T. Improved strength and ductility of Ti₂(CrFeNi)₉₈ multi-principal element alloy at cryogenic temperature with deformation twins induced by BCC precipitates. *Mater. Sci. Eng. A* **2023**, *862*, 144489. [[CrossRef](#)]
68. Tang, K.; Wu, Y.K.; Wei, R.; Chen, L.B.; Lu, S.; Qi, Y.L.; Jiang, F.; Sun, J. Achieving superior cryogenic tensile properties in a Ti-doped (Fe₄₀Mn₄₀Co₁₀Cr₁₀)_{96.7}C_{3.3} high-entropy alloy by recovering deformation twinning. *Mater. Sci. Eng. A* **2021**, *808*, 140927. [[CrossRef](#)]
69. Chen, L.; Li, Z.; Dai, P.; Fu, P.; Tang, Q.; Chen, J. Microstructure and tensile properties of metastable Fe₅₀Mn₃₀Co₁₀Cr₁₀ high-entropy alloy prepared via powder metallurgy. *J. Alloys Compd.* **2023**, *955*, 170225. [[CrossRef](#)]
70. Kim, D.G.; Jo, Y.H.; Yang, J.; Choi, W.-M.; Kim, H.S.; Lee, B.-J.; Sohn, S.S.; Lee, S. Ultrastrong duplex high-entropy alloy with 2 GPa cryogenic strength enabled by an accelerated martensitic transformation. *Scr. Mater.* **2019**, *171*, 67–72. [[CrossRef](#)]

71. Yang, T.; Zhao, Y.; Tong, Y.; Jiao, Z.; Wei, J.; Cai, J.; Han, X.; Chen, D.; Hu, A.; Kai, J.; et al. Multicomponent intermetallic nanoparticles and superb mechanical behaviors of complex alloys. *Science* **2018**, *362*, 933–937. [[CrossRef](#)]
72. He, J.; Fukuyama, S.; Yokogawa, K. Deformation bands in Inconel 718. *Mater. Sci. Technol.* **1995**, *11*, 914–920. [[CrossRef](#)]
73. Yoo, J.; Park, K.-T. Microband-induced plasticity in a high Mn–Al–C light steel. *Mater. Sci. Eng. A* **2008**, *496*, 417–424. [[CrossRef](#)]

Disclaimer/Publisher’s Note: The statements, opinions and data contained in all publications are solely those of the individual author(s) and contributor(s) and not of MDPI and/or the editor(s). MDPI and/or the editor(s) disclaim responsibility for any injury to people or property resulting from any ideas, methods, instructions or products referred to in the content.